Atmospheric Research 296 (2023) 107072

Contents lists available at ScienceDirect

Atmospheric Research

journal homepage: www.elsevier.com/locate/atmosres

Analysis of the solar radiation/atmosphere interaction at a Mediterranean site: The role of clouds

Ismael L. Lozano [a,b,*], Inmaculada Alados [c,d], Inmaculada Foyo-Moreno [d,e]

[a] *Department of Forest Sciences, University of Helsinki, Helsinki 00014, Finland*
[b] *Institute for Atmospheric and Earth System Research, University of Helsinki, Helsinki 00014, Finland*
[c] *Departament of Applied Physics II, University of Málaga, Málaga 29071, Spain*
[d] *Andalusian Institute for Earth System Research, Granada 18006, Spain*
[e] *Department of Applied Physics, University of Granada, Granada 18071, Spain*

ARTICLE INFO

Keywords:
Cloud radiative forcing
Direct/diffuse partitioning
Photosynthetically active radiation
Total solar irradiance spectrum

ABSTRACT

This study is the last of a series of three research papers analysing the solar radiation and its interaction with the atmospheric components spanning an eleven-year period (2008–2018) at a mid-latitude urban site in the Mediterranean basin. During the previous works a detailed characterization of the photosynthetically active radiation (PAR; 400–700 nm), as well as analysis the aerosol and clouds effects on PAR was carried out. This research work addresses an analysis of solar radiation on the total solar irradiance spectrum (TSI; 280–3000 nm) in terms of the effects of different atmospheric conditions on it, considered by the clearness index and the cloud cover, bringing very valuable findings from the long-term comparative analysis of radiative effects of clouds on TSI and PAR wavelength ranges. The average values in the entire period of the study for the global solar radiation in the total solar irradiance (TSI_{Global}) found to be 450 ± 100 Wm^{-2} and 530 ± 110 Wm^{-2} under all and clear-sky conditions, respectively. Meanwhile, the average values for the diffuse component ($TSI_{Diffuse}$) are 141 ± 21 Wm^{-2} and 130 ± 21 Wm^{-2} (all and clear skies, respectively), with a relatively low interannual variation up to 11% for both global and diffuse TSI, as well as for both sky conditions. Analysis on the total cloud cover (TCC) shows that the clearness index is not a good parameter to discriminate between all and clear sky conditions, since there is a marked overlap in the ranges of the k_t values for the different categories of TCC. Additionally, the cloud radiative forcing (CRF) are computed as the difference in solar radiation measured under all and clear sky conditions. A high seasonal variability is found for CRF, where $CRF_{TSI,Global}$ ranges between −37.6 Wm^{-2} and -137.4 Wm^{-2}, while $CRF_{TSI,Diffuse}$ from 4.4 Wm^{-2} to 22.6 Wm^{-2}. The positive sign implies increase in solar radiation at the surface, while the negative one implies the opposite, i.e., less availability of solar radiation on the surface. Finally, the analysis of the annual evolution of CRF reveals a downward trend on CRF_{TSI} and CRF_{PAR}, for both global and diffuse This relevant finding implies that clouds are exerting less cooling effects over time at this Mediterranean site.

1. Introduction

Solar radiation at the surface is a key component for the Earth's energy budget; moreover, solar radiation is the main driver for climate (Stocker et al., 2013; Trenberth et al., 2009), and an essential source or energy for life (Wild, 2009). For this reason, a deepening in the knowledge of the atmosphere/solar radiation interaction is a key parameter to understand changes in the energy budget and its effect over the Earth. Furthermore, recent studies found that the impact of solar radiation over the CO_2 uptake and plants productivity is more important than temperature or other environmental factors (Gonsamo et al., 2015; Liu et al., 2021). Hence, it is not a coincidence that the conclusions of some studies characterise solar radiation, in the photosynthetically active radiation range (PAR), as a modulator of Greenhouse Gases's (GhGs) emission in the atmosphere by crops (Keane et al., 2017; Roebroek et al., 2020; Tan et al., 2018), as PAR exerts control over the biogeo-ecological processes, e.g., hydrological cycles and carbon cycle (Jonard et al., 2020; Potter et al., 2008a, 2008b).

Interactions between atmospheric components (aerosol particles, gases and clouds) controls not only the availability of solar radiation on

* Corresponding author at: Department of Forest Sciences, University of Helsinki, Helsinki 00014, Finland.
E-mail address: ismael.lozano@helsinki.fi (I.L. Lozano).

https://doi.org/10.1016/j.atmosres.2023.107072
Received 17 July 2023; Received in revised form 20 October 2023; Accepted 20 October 2023
Available online 21 October 2023

the surface but also its partition into its diffuse and direct components, as well as its spectral composition (Gu et al., 2002; Lozano et al., 2022; Lukáč, 1994; Mercado et al., 2009). Clouds are considered the most important modulating factor that determines the spatial and temporal availability of solar radiation on the surface as well as its partitioning in the direct/diffuse components. However, the effect of aerosols and clouds on solar radiation and its consequences on climate remains unclear (Cohan et al., 2002; Lozano et al., 2021; Mekic and Gligorovski, 2021; Stocker et al., 2013; Yu et al., 2022), also, the response of clouds to global warming is a high source of uncertainty (Schneider et al., 2017).

In the scientific literature it is relatively common to find extensive studies on clouds radiative forcing (CRF), since it plays a relevant role in the general atmospheric circulation, and further in the climatic variability; for example, changes in CRF have the capability to modify the amplitude/duration and periodicity of the El Niño-southern oscillation (Middlemas et al., 2019; Rädel et al., 2016). However, the total cloud cover (TCC) from 1970 to present is relatively stable, making more interesting to focus on regional scale since strong fluctuations have been found during the last decades at regional scale (Eastman and Warren, 2013; Warren et al., 2007).

Focusing on a more local scale, during the last decades in the Mediterranean region, a faster temperature increase has been reported than in the world average (Lionello et al., 2014; Lionello and Scarascia, 2018) while an increase in extreme climatic events is predicted (e.g., heat waves, droughts; Garcia-Herrera et al., 2014; Lionello et al., 2014) making this region a suitable laboratory for CRF and its climatic effects. In fact, heatwave episodes are becoming more frequent and severe in different parts of the world and especially in the Mediterranean region (Delgado-Capel et al., 2023), with high impact in cities. In this context, the present study is the last of a series of three works analysing long-term trends in aerosol (Lozano et al., 2021) and long-term CRF (Lozano et al., 2022) at an urban mid-latitude site of the South-east of Spain in the Mediterranean basin, covering eleven years (2008 to 2018). The first study was focussed on the study of the long-term aerosol radiative forcing on TSI (280–3000 nm) and PAR (400–700 nm) radiations, in which the two main findings were (i) the PAR range is more sensitive to changes in aerosols, and (ii) the cooling effect of aerosols are significantly decreasing in this Mediterranean site over time. The second study analysed CRF on global and diffuse PAR in which we related the diffuse CRF pattern with the annual pattern observed in the frequency of high clouds and the content of total ice water in clouds. Another finding was the establishment of a relation between the diffuse fraction of PAR (k_{PAR}) and the clearness index in the total solar irradiance (k_t) leading to the possibility of predicting the diffuse component of PAR using only measurements in the total solar irradiance spectrum.

The aim of the present study is to analyse the clouds effects over the solar radiation for both global and in diffuse components in a series of long-term data (2008–2018), for clear skies as well as for all skies. For this goal, $TSI_{Diffuse}$ is derived from an empirical model (Ridley et al., 2010), then a complete statistical analysis of TSI_{Global} and $TSI_{Diffuse}$ is carried out, analysing its distribution and density versus different atmospheric conditions. Additionally, the distribution of k_t and the diffuse fraction (k) is analysed versus TCC and also by the solar radiation path through the atmosphere. Finally, a comparative analysis between global and diffuse CRF in both TSI and PAR ranges is evaluated, ending with an analysis of its trends over time at this Mediterranean site.

2. Experimental site and data acquisition

2.1. Experimental site

The radiometric station at the IISTA-CEAMA building, University of Granada, is located in Granada (37.16°N, 3.61°W, 680 m a.s.l.), a non-industrialized city in the Mediterranean basin (Southeast of Spain). This station is part of the AGORA observatory (Andalusian Global ObservatoRy of the Atmosphere) and is within ACTRIS framework (Aerosol, Clouds and Trace Gases Research Infrastructure). Granada has a continental Mediterranean climate characterized by dry and hot summers, and cold winters, with daily maximum and minimum mean temperatures of 32 ± 3 °C and 14.6 ± 2.4 °C, respectively (AEMET, Spanish Meteorology Statal Agency; period 1981–2010). The city is surrounded by mountains and is located in the foothills of Sierra Nevada Mountain (Mulhacen peak at 3482 m a.s.l.). The orography favours thermal inversions in winter and prevalence of low wind speeds (Lyamani et al., 2012), and allow long residence time and coexistence of different sources of aerosols in the atmosphere: (i) local aerosol from mineral dust, traffic, domestic heating, and bioaerosols (Cariñanos et al., 2021; Ramírez-Aliaga et al., 2022; Titos et al., 2017), and (ii) allochthonous aerosols mainly from Saharan dust, anthropogenic pollution from Europe, transported smoke from North America and Europe, oceanic and maritime aerosols, and occasionally volcanic plumes (Alados-Arboledas et al., 2011; Guerrero-Rascado et al., 2009; Lyamani et al., 2006a, 2006b; Navas-Guzmán et al., 2013; Ortiz-Amezcua et al., 2017; Pérez-Ramírez et al., 2015).

2.2. Radiation measurements

Two datasets of solar radiation are employed in this study: (i) a first dataset, named the study dataset, in which all analyses are performed, and is composed of 11-year (2008–2018) measurements of PAR_{Global} (400–700 nm wavelength) and TSI_{Global} (280–2800 nm wavelength) radiation, and (ii) a second dataset employed to evaluate the fitting coefficients to be applied in the first dataset to estimate the diffuse component of the solar radiation, and is composed of 2-years measurements (1994–1995) of PAR and TSI, both in global and diffuse components. The data from the first dataset were collected by a SKP 215 PAR Quantum Sensor manufactured by Skye Instruments (Wales, UK), and a CM11 radiometer manufactured by Kipp and Zonen (Delf. Netherlands). The quantum sensor has a sensitivity of 0.015 $\mu A \mu mol^{-1} m^{-2} s^{-1}$ and a maximum relative error of ±5%, while the pyranometer has a maximum directional error of 10 Wm^{-2}. The instruments were calibrated several times during the eleven years; further details can be followed in Lozano et al. (2021, 2022). Data from the second dataset were collected by two LICOR Li-190SA quantum sensors (Lincoln, USA), and two Kipp and Zonen CM-11 radiometers. The LICOR quantum sensor has a relative error of less than ±5%. One of the LICOR sensor was mounted on the shadow band's polar axis to measure the diffuse component, and these measurements were corrected for the shadow-band effect by the method proposed by Batlles et al. (1995). Further details about the instruments calibration used to record the data in this second database can be found in Foyo-Moreno et al. (2018), Lozano et al. (2022), and Alados and Alados-Arboledas (1999).

To guarantee the data quality an in-deep control test was carried out to detect and remove anomalous, low accurate and potential erroneous measurements, following Lozano et al. (2022). First of all, those solar radiation measurements corresponding to solar zenith angle (θ) below 80° were only considered, in order to avoid the cosine response error. Secondly, solar radiation values were taken into account for $kt < 1$. The clearness index is defined as the ratio of the global to the extraterrestrial irradiance on a horizontal surface, and can be computed for the different spectral ranges considered in this study, i.e., TSI (k_t) or PAR ($k_{t,PAR}$). Thirdly, a visual inspection of the data was performed to detect and remove outliers and power supply failures or temperature malfunctioning. A conversion factor of 4.57 $\mu mol^{-1} m^{-2} s^{-1}$ / Wm^{-2} (McCree, 1972) were applied to the PAR measurements to convert PAR from photons measurements to energy units.

2.3. Cloud data

In this study we employ total cloud cover (TCC) data for the complete study period (2008–2018) from the European Centre for Medium-range

Weather Forecasts (ECMWF) Reanalysis Fifth Generation (ERA5) database. This reanalysis has been generated from a process that involves observations, satellite, aircraft and surface data (Copernicus Climate Change Service (C3S), 2017). ERA5 reanalysis provides data with high temporal resolution on a regular longitude-latitude grids (0.25° x 0.25°), and is open access available at the Climate Data Store (https://cds.climate.copernicus.eu/cdsapp#!/home). TCC integrates all clouds (low to high) by employing overlap assumptions (Barker, 2008; Jakob and Klein, 2000). That is, a linear combination of multiple overlapping layers covering the entire column with the weight of each layer defined by the distance between layers. Assumptions are made about the degree of overlap/randomness between clouds at different heights. Cloud fractions vary from 0 to 1 (Jakob and Klein, 2000). The Cloud data from ERA5 has a relative error below ±10% with respect to MODIS, and special good behaviour for latitudes between 0° and 30° (North and South).

3. Methods

3.1. Modelling the diffuse component of solar radiation

In this study, the diffuse component of the solar radiation was obtained from the estimation of the diffuse fraction (k), defined as the ratio of the diffuse to the global irradiance on a horizontal surface; it has a well-known relationship with k_t. Therefore, we use this relationship ($k - k_t$), since estimates of the irradiance ratios have a lower uncertainty than the estimates of the relationship between the absolute values, i.e., diffuse and global irradiance (Badarinath et al., 2007). We employed the so-called BRL model to obtain the diffuse fraction, originally proposed by Ridley et al. (2010) and based on the logistic relationship between k and k_t:

$$k = \frac{1}{1 + exp\left(a_1 + a_2k_t + a_3\alpha + a_4AST + a_5K_t' + a_6\Psi\right)} \tag{1}$$

where a_i are the fitting coefficients, α is the solar elevation in degrees, AST is the apparent solar time, K'_t is the daily clearance index, and Ψ is the persistence index. These two last variables can be computed as follows:

$$K_t' = \frac{\sum_{i=1}^{24} TSI_{Global}}{\sum_{i=1}^{24} I_{TOA}} \tag{2}$$

$$\psi = \frac{k_{t,time-1} + k_{t,time+1}}{2} \tag{3}$$

Following Iqbal (1983), the irradiance at the top of the atmosphere (I_{TOA}) is computed as:

$$I_{TOA} = I_0E_0cos\theta \tag{4}$$

where I_0 is the solar constant (1367 Wm^{-2}; Iqbal, 1983) and E_0 is the eccentricity correction factor of the Earth's orbit, given by Spencer (1971):

$$r_0 = \left(\frac{r_0}{r}\right)^2 = 1.000110 + 0.034221cos\Gamma + 0.001280sin\Gamma + 0.000719cos2\Gamma + 0.000077sin2\Gamma \tag{5}$$

where r and r_0 are the sun-earth and the mean sun-earth distances, respectively, and Γ is called the day angle, given by:

$$\Gamma = \frac{2\pi(d_n - 1)}{365} \tag{6}$$

Where d_n is the day number of the year (1–365).

To obtain k_{PAR} we also employed the BRL model. Although this model was originally proposed to estimate the diffuse component in the total spectrum of solar radiation, it has been previously analysed in different spectral ranges like the UV (Sanchez et al., 2017), or in PAR (Kathilankal et al., 2014; Lozano et al., 2022), its expression is:

$$k_{PAR} = \frac{1}{1 + exp\left(b_1 + b_2k_{t,PAR} + b_3\alpha + b_4AST + b_5K_{t,PAR}' + b_6\Psi_{PAR}\right)} \tag{7}$$

where b_i are the fitting coefficients, $K'_{t,PAR}$ is the daily clearance index, and Ψ_{PAR} is the persistence index, both in the PAR range, and can be computed as follows:

$$K_{t,PAR}' = \frac{\sum_{i=1}^{24} PAR_{Global}}{\sum_{i=1}^{24} I_{TOA,PAR}} \tag{8}$$

$$\Psi_{PAR} = \frac{k_{t,PAR}^{time-1} + k_{t,PAR}^{time+1}}{2} \tag{9}$$

The irradiance at the top of the atmosphere for PAR ($I_{TOA,PAR}$) can be computed as:

$$I_{TOA,PAR} = I_{0,PAR}E_0cos\theta \tag{10}$$

Where $I_{0,PAR}$ is the solar constant in the PAR range (634.4 Wm^{-2}; Iqbal, 1983).

For both spectral ranges, the diffuse fraction was estimated by employing the second dataset described in Section 2.2. This dataset was randomly divided into two subsets, the first one with the 75% of the data, in order to obtain the fitting coefficients, and the remaining 25% of the data for validation. Table 1 shows the fitting coefficients for both spectral ranges and the root mean square error (RMSE), the mean bias error (MBE) and the coefficient of determination (r^2) computed from the validation dataset. The model shows the good performance for both spectral ranges with an $r^2 \geq 0.80$, for TSI, and very low values of MBE ($\leq$ 0.008) and RMSE ($\leq$ 0.11), the MBE and RMSE values are within the ranges reported in the literature for different locations, including the same site (in the PAR range) (Jacovides et al., 2010; Kathilankal et al., 2014; Lozano et al., 2022; Ridley et al., 2010).

3.2. Cloud radiative forcing

In this study, the cloud effects on solar radiation have been assessed by the so-called Cloud Radiative Forcing (CRF) analysis, computed as the difference between solar radiation in all and clear sky conditions (Harrison et al., 1990; Ramanathan et al., 1989):

$$CRF = I_{All} - I_{Clear} \tag{11}$$

where I is the experimental irradiance, and can be computed in the TSI (CRF_{TSI}) or PAR (CRF_{PAR}) ranges.

Considering the CRF definition, a differentiation between clear and

Table 1
Fitting coefficients obtained from k and k_{PAR} modelling, and solar radiation statistic obtained from the validation process.

Fitting Coefficients			
ai	k	bi	k_{PAR}
a1	−8.05 ± 0.13	b1	−5.98 ± 0.09
a2	8.16 ± 0.15	b2	7.89 ± 0.23
a3	0.215 ± 0.006	b3	0.004 ± 0.005
a4	−0.002 ± 0.001	b4	0.006 ± 0.001
a5	−0.14 ± 0.22	b5	0.98 ± 0.21
a6	1.41 ± 0.16	b6	2.1 ± 0.3
	Statistics		
RMSE (Wm^{-2})	0.11		0.10
MBE (Wm^{-2})	0.004		0.008
r^2	0.80		0.87

all sky conditions is necessary in this study. Therefore, to extract clear skies, the Long and Ackerman (2000) tests (number one and number three) were applied. These two tests identify clear skies by analysing the normalized TSI and the differences in the range of variation of the TSI irradiance at the surface with respect to the TOA. The first test normalized the downwelling TSI using a power function of the θ:

$$TSI_N = \frac{TSI}{\theta^b} \tag{12}$$

where TSI_N is the normalized TSI, and b is a constant. Then a maximum and minimum value are set for TSI_N, and only the normalized data inside these ranges are considered. These maximum and minimum needs to be set experimentally. The third test consider that TSI on the surface is always lower than in the top of the atmosphere due to the attenuation process by the atmosphere, and compare the changes in the TSI with respect to the changes in the I_{TOA} (in absolute terms), i.e., the difference between the values previous and following to the measurement of interest of both variables: $|\Delta TSI/\Delta t|$ and $|\Delta I_{TOA}/\Delta t|$. Therefore, only the values of $|\Delta TSI/\Delta t|$ within a maximum and minimum value are considered. This range are defined as follow:

$$MIN = \left|\frac{\Delta I_{TOA}}{\Delta t}\right| + C\theta \tag{13}$$

$$MAX = \left|\frac{\Delta I_{TOA}}{\Delta t}\right| - \left[R_t(\theta^{noon} + 0.1)/\theta\right] \tag{14}$$

where C is a subjective constant observed in the data being processed, R_t is the temporal resolution of the data in minutes, and θ^{noom} is the solar zenith angle at noon. See Long and Ackerman (2000) for further details.

Additionally, we performed a visual inspection in the whole dataset in order to detect any misclassified data points, instead of using Long and Ackermand tests number two and four due to the absence of diffuse measurements in this dataset needed to perform both tests.

3.3. Data analysis

Once the fitting coefficients were obtained from the second subset of data, the $TSI_{Diffuse}$ and $PAR_{Diffuse}$ time series were rebuilt on the first subset of data (study dataset). After that, a complete statistical analysis was performed by the arithmetic mean (Mean), standard deviation (SD), median (Md), minimum (Mi) and maximum (Ma) values, percentiles 5th, 25th, 75th, and 95th (P5, P25, P75, P95, respectively), skewness (Ske), and kurtosis (kur), for both clear and all sky conditions, summarized in Table S1 in the supplementary materials.

Finally, to detect trends in the CRF time series, the Mann-Kendall's (Mann, 1945) non parametric test was applied; to evaluate the slope in this time series, the Sen estimation method (Sen, 1968) was used by employing the kbtau.m software developed by Jeff Burkey (2020) to perform the calculations. The Sen method, and the Mann-Kendall's test are not affected by outliers or gaps and, therefore, they are commonly used in the scientific literature (e.g., Buffoni et al., 1999; Kambezidis, 2021; Kodera et al., 2008; Kuo et al., 2020; Lozano et al., 2021; Zou et al., 2016).

4. Results and discussion

4.1. Total solar radiation time series

The average values observed for the entire study period (2008–2018) were 450 ± 100 Wm^{-2} and 530 ± 110 Wm^{-2} for TSI_{Global} under all and clear sky conditions, respectively (i.e., the mean value of the global radiation is 20% higher under clear skies condition), meanwhile for $TSI_{Diffuse}$ the average values were estimated at 141 ± 21 Wm^{-2} and 130 ± 21 Wm^{-2} for all and clear skies, respectively (i.e., the mean value of the diffuse component is 9% lower under clear skies condition). As it is expected, the maximum values for TSI_{Global} have been obtained under clear skies considering that clouds are the main attenuators of solar radiation, the diffuse component is higher because of increased scattering processes in cloudy conditions. On average, the ratio of diffuse to global radiation is 31% for all skies and 25% for clear skies. Fig. 1 shows the TSI times series of monthly mean values for both TSI_{Global} and $TSI_{Diffuse}$, with differentiation between all and clear sky conditions; Fig. 2 displays a boxplot with statistical information about the monthly values.

From Fig. 1, as it was expected, a clear seasonal pattern is detected in both TSI_{Global} and $TSI_{Diffuse}$ under both sky conditions, with higher values during the warmer months and lower values during the colder ones, this seasonal pattern can also be observed in Fig. 2, and is mainly due to the differences in the course of solar zenith angle during the year, with the prevalence of higher values in the wintertime. Thus, TSI_{Global} reach its maximum value of 620 ± 30 Wm^{-2} for all skies in July 2018 and 720 ± 90 Wm^{-2} for clear skies in May 2013, while for $TSI_{Diffuse}$ maximum values are about 185 ± 24 Wm^{-2} in July 2016 for all skies and about 187 ± 21 Wm^{-2} in June 2018 for clear skies. The minimum values for TSI_{Global} are 250 ± 100 Wm^{-2} reached in January 2009 for all skies and 350 ± 40 Wm^{-2} in December 2011 for clear skies, meanwhile the value for $TSI_{Diffuse}$ is 98 ± 15 Wm^{-2} in December 2017 for all skies, and 82 ± 17 Wm^{-2} in February 2013 for clear skies. As expected, TSI_{Global} reached higher values over clear sky conditions, while $TSI_{Diffuse}$ reached high values in all skies ones, due to the scattering processes in the atmosphere related to cloudy weather.

Additionally, a remarkable intra-annual variability between maxima and minima monthly mean value has been observed, being the higher differences in TSI_{Global} of 84% (2009) and 67% (2013), while in $TSI_{Diffuse}$ this is about 48% (2015) and 69% (2013) for all and clear sky conditions, respectively. Thus, the highest variability is found for TSI_{Global} in clear skies and for $TSI_{Diffuse}$ in all sky conditions (although less than TSI_{Global}). On the other hand, the inter-annual variability between the maximum and minimum annual averages observed in the period 2008–2018 shows values of 46 Wm^{-2} (10% of variation) and 35 Wm^{-2} (7% of variation) for TSI_{Global} under all and clear sky cases, respectively, while for $TSI_{Diffuse}$ theses values are 12 Wm^{-2} (9% of variation) and 14 Wm^{-2} (11% of variation), under all and clear skies, respectively, which imply a maximum interannual variation of 11% in total solar radiation under all sky conditions.

In the same period and study site Lozano et al. (2022) performed a similar analysis of the solar radiation time series in the PAR range, and they found similar patterns, as may be expected, i.e., similar differences in the study period mean values between all and clear skies, in

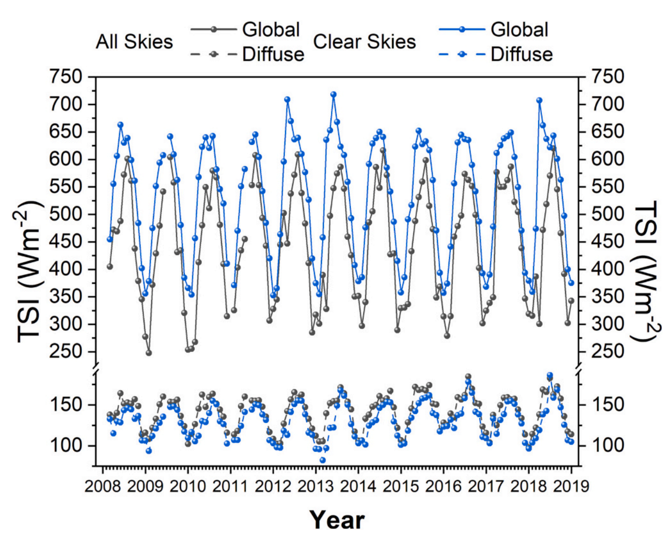

Fig. 1. Time series of monthly mean TSI_{Global} (solid lines) and $TSI_{Diffuse}$ (dashed lines) for all sky conditions in the entire experimental period (2008–2018).

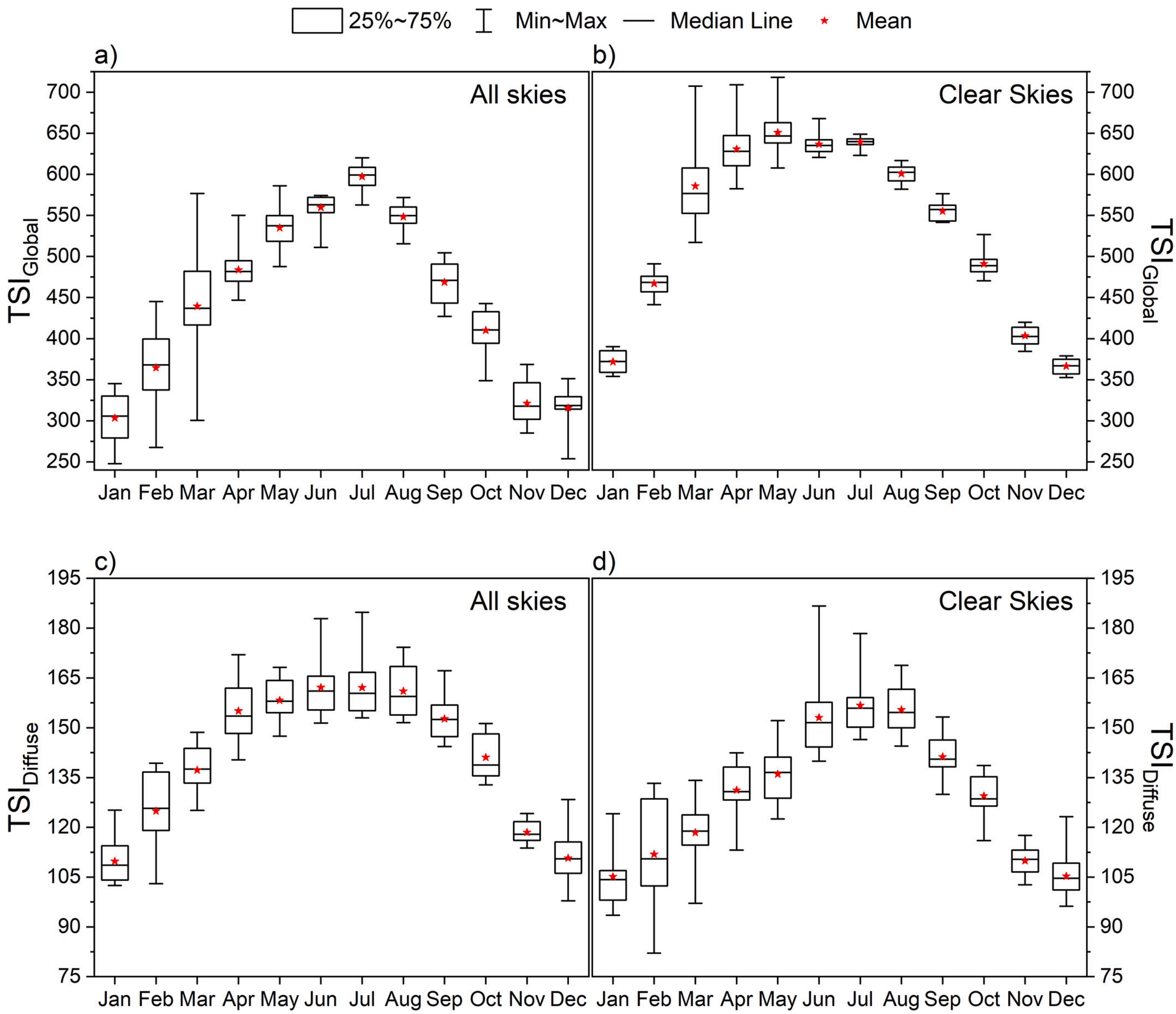

Fig. 2. Monthly statistics in 2008 to 2018 period at Granada, for TSI_{Global} under (a) all- and (b) clear- sky conditions, and for $TSI_{Diffuse}$ under (c) all- and (d) clear- sky scenarios. Central line of each box is the median, stars are the average value, limits of the box are the percentiles 25th and 75th, and limits of the segments represent the minimum and maximum monthly mean values.

percentage, for PAR_{Global} (17% less instead of 20%); meanwhile the differences for the diffuse component were significatively higher (16% more, instead of 9%). In addition, they found an interannual variation up to 20% in the PAR range that is clearly nearly double the interannual variability in the total solar irradiance spectrum. Other authors have analysed the TSI_{Global} in all the Mediterranean basin; Pyrina et al. (2015) found a TSI_{Global} mean values ranging from 170-180 Wm^{-2} to 480 Wm^{-2} in a period of 24 years (1984–2007), these values are lower than our results by 39–47% or 29%, respectively. These differences are reasonable considering the variability of environments in the Mediterranean basin. Meloni et al. (2015) found values of 534.2 ± 2.2 Wm^{-2} and 101.5 ± 3.5 Wm^{-2} (measured at a fixed latitude of 55.9 ± 0.25°) on 3 May 2008 for TSI_{Global} and $TSI_{Diffuse}$, respectively.

The seasonal cycle for TSI_{Global} has a maximum median value of 601 Wm^{-2} in July and its minimum value of about 308 Wm^{-2} in January under all sky conditions, while for clear skies the maximum median value observed is about 643 Wm^{-2} reached in May and the minimum value of 367 Wm^{-2} in December. The behaviour of TSI_{Global} under all sky conditions shows a relative high variability ranging from 3% in the warmers months, to 17% in March (spring); this behaviour is a consequence of the interaction of solar radiation with clouds that also reinforce the effect of the annual course of solar position making more variable its values in the spring season. Precisely, Lozano et al. (2022) found that the maximum values of TCC, total column cloud liquid water, and total column cloud ice content for the same period and city in March. On the contrary, under clear sky conditions this variability is lower, reaching its maximum value in March (9%). On the other hand, the seasonal pattern for $TSI_{Diffuse}$ reached its maximum median value of 160 Wm^{-2} and 155 Wm^{-2} in June and July, respectively, with minimum values of 107 Wm^{-2} and 103 Wm^{-2} in January, under all and clear sky conditions, respectively. The variability of $TSI_{Diffuse}$ reached its maximum value in February for both, all and clear skies, and counter-intuitively, the higher values were under clear skies scenarios (14%), while for all skies the maximum value reached 10%. Lozano et al. (2022) also found February as the month with higher variability in the values of $PAR_{Diffuse}$ for Granada in the same period, as a consequence of winter-time extreme dust events over this city (Cazorla et al., 2017; Fernández et al., 2019). In fact, Lozano et al. (2021) found a relatively high median value of AOD at 500 nm of 0.66 in Granada for the same period. Comparing our results in the $TSI_{Diffuse}$ range with those obtained by Lozano et al. (2022) for the same parameter and period is interesting to note that they found a less marked but more complex seasonal patterns as can be seen in the range of variability, up to 20% under clear sky conditions, reached in February and March. These findings may reinforce the concept that PAR range is more sensitive to atmospheric aerosol effects than TSI (Lozano et al., 2021).

4.2. Atmospheric effects on solar radiation

The effects of the interaction between the atmosphere's components (particles of aerosols, clouds, and gases) and solar radiation in its path through the atmosphere have been considered in the present study by analysing two controlling parameters: the clearness index (k_t) and the total cloud cover (TCC). High values of k_t are associated with clear sky conditions, since this implies a high transparency of the atmosphere. Thus, some authors employ k_t limits to determine clear sky conditions (i. e., $k_t > 0.7$; Ianetz et al., 2007; Ma and Iqbal, 1984). Low values of k_t represent the opposite situation, as low atmospheric transparency is usually associated with cloudy conditions. On the other hand, although k_t includes both effects (aerosols and clouds), the cloud's presence is explicitly quantified by TCC.

Firstly, our analysis will focus on the atmospheric transparency, Fig. 3 shows the relationship between TSI_{Global} and $TSI_{Diffuse}$ with respect to k_t (Fig. 3a and b, respectively) and k (Fig. 3c and d, respectively). The bin-average values are also shown in the figure. These mean values were computed by dividing the x-axis into intervals of 0.1 width, as follows:

$$Bin-average(a,b) = \frac{1}{N}\sum_{i=1}^{N} y_i \tag{15}$$

where a,b represents consecutive intervals [a,b] of increments, of 0.1 amplitude (i.e., 0.1, 0.2, …, 1), N is the total number of data in the interval [a,b], and y_i is the considered variable in the y-axis. These bin-average values aid in the visualization and analysis of the data distribution.

In this figure, the well-known dependence of solar radiation on k_t and k can be seen, as expected. TSI_{Global} grows with k_t, while $TSI_{Diffuse}$ grows to the central values of k_t (close to 0.45) and then decreases. It is interesting to note that the higher data density (represented by the deepest red colours in Fig. 3) can be observed for k_t values approximately between 0.5 and 0.8 for TSI_{Global}, and between 0.7 and 0.8 for $Total_{Diffuse}$. The bin-averaged values range from (60 ± 30 Wm^{-2} to 820 ± 170 Wm^{-2} for TSI_{Global} and from 26 ± 15 Wm^{-2} to 180 ± 90 Wm^{-2} for $TSI_{Diffuse}$. Taking into consideration the representation against k, TSI_{Global} decreases with increase in k, showing a clear linear negative trend in the bin-averaged dots, while in the case of $TSI_{Diffuse}$ there is a growth pattern until approximately 0.3 of k, and then the bin-average values remain more or less constant. This implies that higher values of k are more related to lower values of global radiation, while this is not true for the diffuse component. Then, when the atmosphere is less transparent, there is reduced availability of both TSI_{Global} and $TSI_{Diffuse}$. The bin-average values range from 690 ± 170 Wm^{-2} to 60 ± 30 Wm^{-2} for TSI_{Global} and from 60 ± 30 Wm^{-2} to 180 ± 70 Wm^{-2} for $TSI_{Diffuse}$.

Secondly, it is important to take into consideration not only the atmospheric transparency but also the path of the solar radiation into the atmosphere; therefore, we focus our analysis now on the solar zenith angle (θ). Fig. 4 shows the relationship between TSI_{Global} and $TSI_{Diffuse}$ with respect to θ in the upper panels (Fig. 4a, and b, respectively) and between k_t and k versus θ in the lower ones (Fig. 4c and d, respectively). The averaged values for different variables versus θ range from 180 ± 60 Wm^{-2} to 790 ± 160 Wm^{-2} for TSI_{Global}, and for $TSI_{Diffuse}$ from 100 ± 40 Wm^{-2} to 210 ± 60 Wm^{-2}. In the case of the index ratios versus θ, k_t ranges from 0.49 ± 0.16 to 0.72 ± 0.12, meanwhile k ranges from 0.25 ± 0.17 to 0.6 ± 0.3. As the absolute values of solar radiation are concerned, a marked decreasing trend can be seen for the density plots and also for the bin-averaged values with a higher slope for the global than for the diffuse component. k only shows a positive relationship with the bin-averaged values. The amplitude of the density has very low amplitude for lower values of θ, but this grows with θ. These results imply that

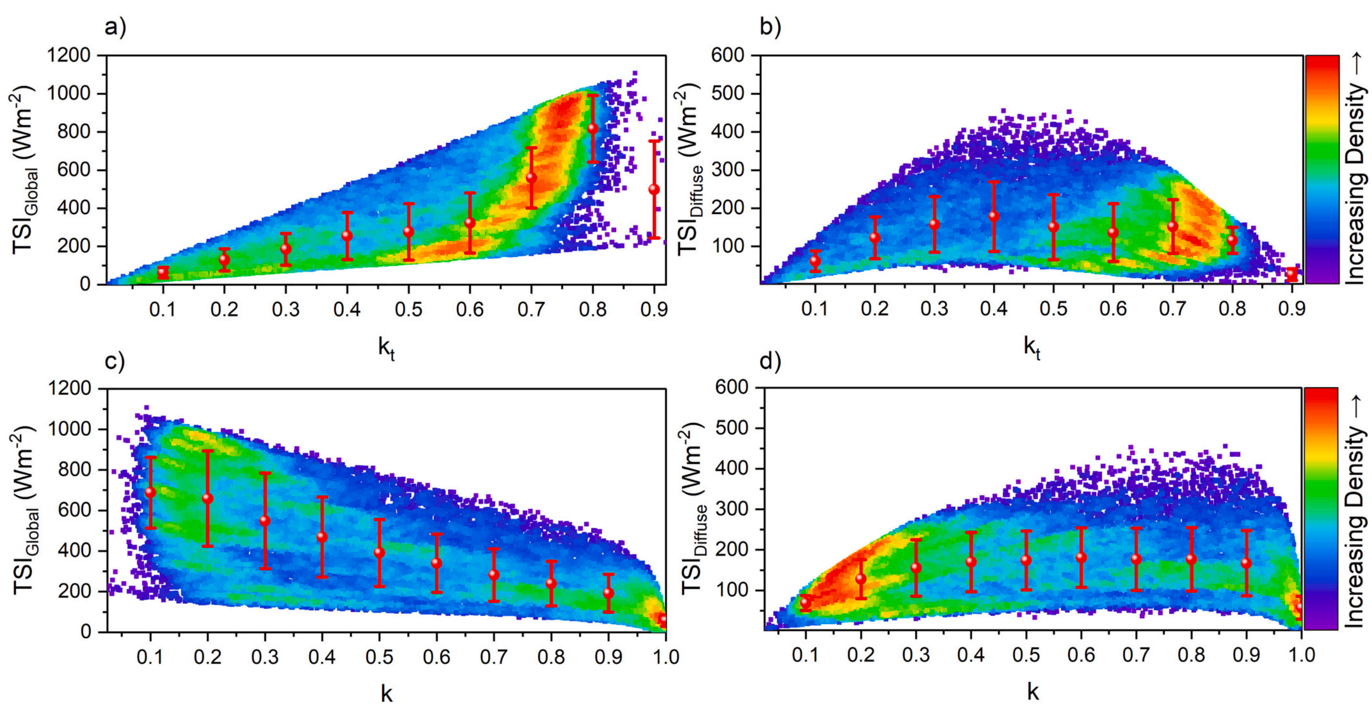

Fig. 3. Relationship between TSI_{Global} (left) or $TSI_{Diffuse}$ (right) versus k_t (upper panels) and k (lower panels) at Granada during the entire study period (2008–2018). The red dots and red bars represent the average values and standard deviation at the k_t and k values indicated. (For interpretation of the references to colour in this figure legend, the reader is referred to the web version of this article.)

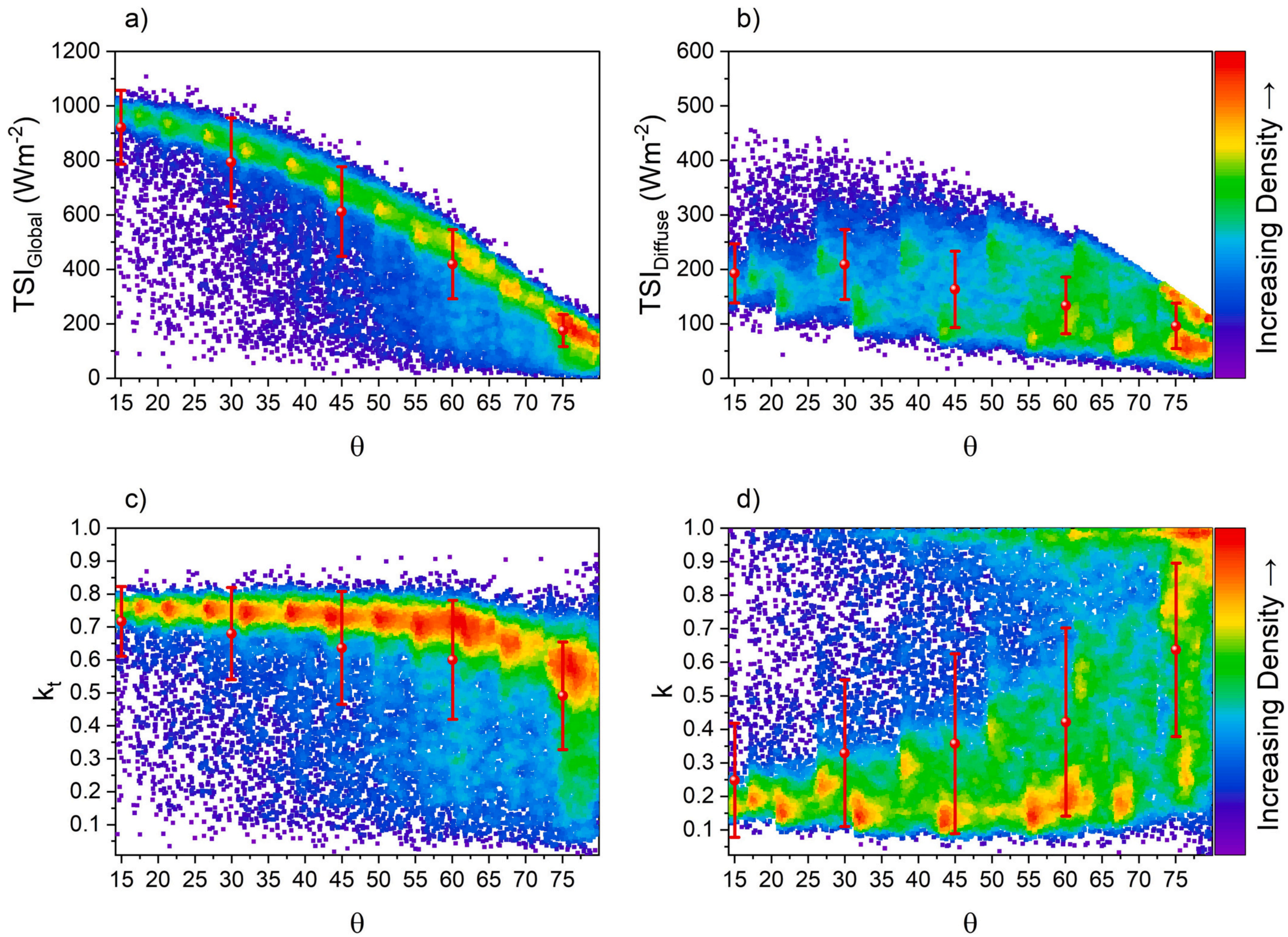

Fig. 4. Relationship between TSI_{Global} (left) or $TSI_{Diffuse}$ (right) versus solar zenith angle (θ) (upper panels), and k_t (right) or k (right) versus θ (lower panels) at Granada during the entire study period (2008–2018). The red dots and red bars represent the average and standard deviation values at the θ values indicated. (For interpretation of the references to colour in this figure legend, the reader is referred to the web version of this article.)

higher values of k do not necessary correspond to larger values of $TSI_{Diffuse}$, specially for high values of θ. On the other hand, k_t does not shows a clear relationship with θ; however, both the bin-averaged values and the area of higher density in the scatter plots follow a decreasing trend versus θ, with a more or less soft slope until the value of 0.6 of θ and then a steeper slope. Secondly, a large spread is observed between k_t versus θ and k versus θ. This is evidenced by the high standard deviation in the bin-average intervals, which reaches values up to ±0.18 and ± 0.28 for k_t and k, respectively.

Focusing on the annual variability of k_t and k, Fig. 5 presents the statistical analysis of the monthly values of k_t (Fig. 5a and b, respectively) and k (Fig. 5c and d, respectively) for both skies cases, where a clear annual behaviour can be observed with higher values in the warmer months and minimum values in the colder ones for k_t reaching up to 0.67 in July and 0.72 in April, and with minimum values of 0.53 in November and 0.67 in December for all and clear sky conditions, respectively. The opposite behaviour is observed in k, reaching minimum values in the warmer months, 0.33 in July and 0.26 in March, for all and clear sky conditions, respectively, and with maximum values during wintertime, reaching values of 0.53 in November under all, and 0.32 in December under clear sky conditions. Focusing on all skies, this behaviour is related to the higher TCC and higher frequency of overcast skies that match the higher values of k and lower ones of k_t, as can be seen in Fig. 6. On the other hand, in the summer higher sunshine duration due to lower TCC favours higher values of k_t and lower ones of k. In the case of clear sky conditions (Fig. 5b) a growing trend can be found up to the spring and then the slope shifts to a decreasing trend until the end of the year for k_t, while the opposite exists in the case of the k (Fig. 5d); this behaviour is related to the larger atmospheric paths of solar radiation in winter-time due to lower values of solar elevation angles. It is interesting to note that a secondary maximum value can be found in k under clear skies in August with a value of 0.31, pretty close to the maximum value found in December. Lozano et al. (2022) found the same secondary maximum value for k_{PAR} in August, due to the high occurrence of Saharan dust intrusions events over Granada during summer time (Salvador et al., 2014).

Focusing on the different thresholds for k_t under all and clear sky conditions, there is a prevalence of higher values for clear skies where minimum median monthly values are greater than the maximum values under all skies conditions for most of the months. Besides that, kt under clear sky conditions has quite lower variability than under all sky conditions (Fig. 5b). These are the reasons for k_t to be used as a criterion for discriminating clear sky conditions. However, there is an overlap between minimum median monthly values under clear and maximum median monthly values under all sky conditions in several months, including the warmer ones, and this is a reason why using another criterion to determine clear skies instead of k_t may solve several misclassified data. To solve this issue some authors have employed k in order to classify clear skies, e.g., Lefèvre et al. (2013) proposed to use values of k lower than 0.3 to consider clear skies. Focusing on our k

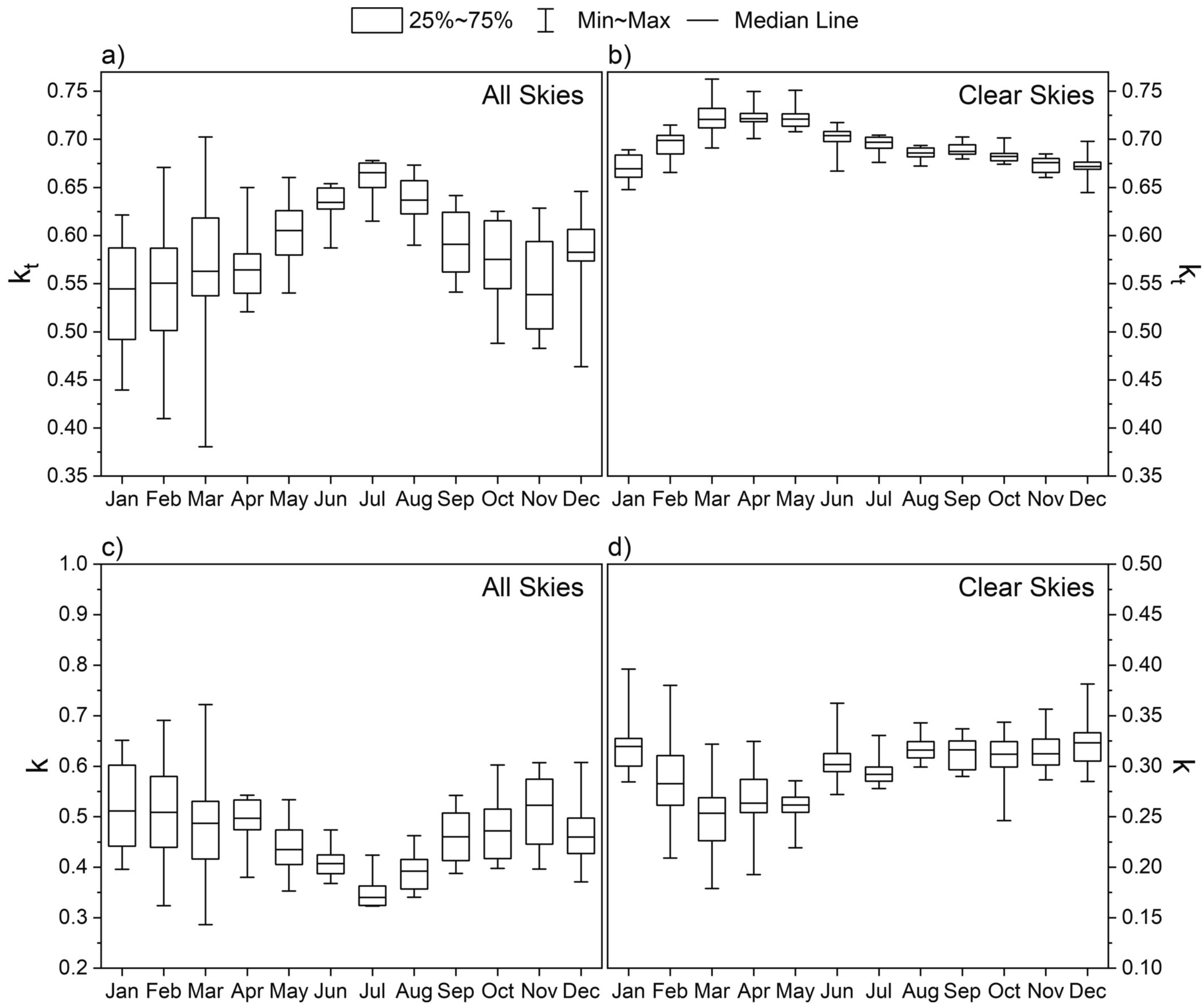

Fig. 5. Monthly statistics in the period 2008 to 2018 at Granada for k_t under (a) all- and (b) clear- sky conditions, and for k under (c) all- and (d) clear- sky ones. The central lines in each box represent the median values, the stars the average values, the upper and lower limits of the boxes the 75th and 25th percentiles, and the upper and lower limits of the bars represent the maximum and minimum monthly mean values.

monthly median values under all skies, only some values under 0.3 were found in spring; then using this threshold may lead to some misclassified data. However, if we focus on clear skies, the prevalence of values over this threshold can be confirmed. Other authors have proposed to use a combination of both, k_t and k, e.g., Thevenard and Brunger (2002a, 2002b) used a k value between 0.2 and 0.4; however, visual inspection of the data is needed to confirm and avoid misclassified data. On the other hand, some authors employ more complex relationships and indexes to determine clear sky conditions; one of the mostly used and considered as standard method is the one proposed by Long and Ackerman (2000). However, the absence of measurements for the diffuse component at most stations make this method difficult to apply, since it needs such measurements in two of its four tests. Recently, Kambezidis et al. (2021) have shown that the condition $0 \leq k \leq 0.26$ determines clear skies at universal scale.

Considering the TCC that controls the variation of solar radiation, Fig. 6 shows the relationship between TSI_{Global} or $TSI_{Diffuse}$ versus TCC (upper panels; Fig. 6a and b, respectively) and also between k_t or k versus TCC (lower panels; Fig. 6c and d, respectively). TSI_{Global} averaged values range from 240 ± 190 Wm^{-2} to 530 ± 260 Wm^{-2} and $TSI_{Diffuse}$ from 140 ± 60 Wm^{-2} to 150 ± 90 Wm^{-2}; meanwhile k_t and k vary from 0.66 ± 0.11 to 0.34 ± 0.19 and from 0.36 ± 0.23 to 0.80 ± 0.23, respectively. Although the TSI_{Global} values shows very high spread versus TCC, and do not seem to follow any trend or pattern, the bin-averaged values follow a downward trend, and their slope, in absolute terms, increases notably for overcast skies (TCC > 0.9). $TSI_{Diffuse}$ also shows very high spread in the scatterplot, especially for overcast skies. However, the bin-averaged values of this variable do not follow any increasing or decreasing trend. In the case of the ratios, k_t and k bin-averaged follows the opposite trend, as expected, a decreasing trend for k_t and an increasing one, and with a higher slope for k. The computed slopes of these trends (not shown in the figure) are −0.31 ± 0.03 and 0.43 ± 0.05 for k_t and k, respectively, with a r^2 over 0.90 in both cases. These high correlations with TCC and also the differences between the mean value for the entire experimental period in both variables (k_t and k) under all and clear skies, are of 0.59 and 0.69 for k_t, and 0.46 and 0.30 for k, for both all, and clear skies, respectively. This highlights the relevant role of clouds not only in the availability of solar radiation on

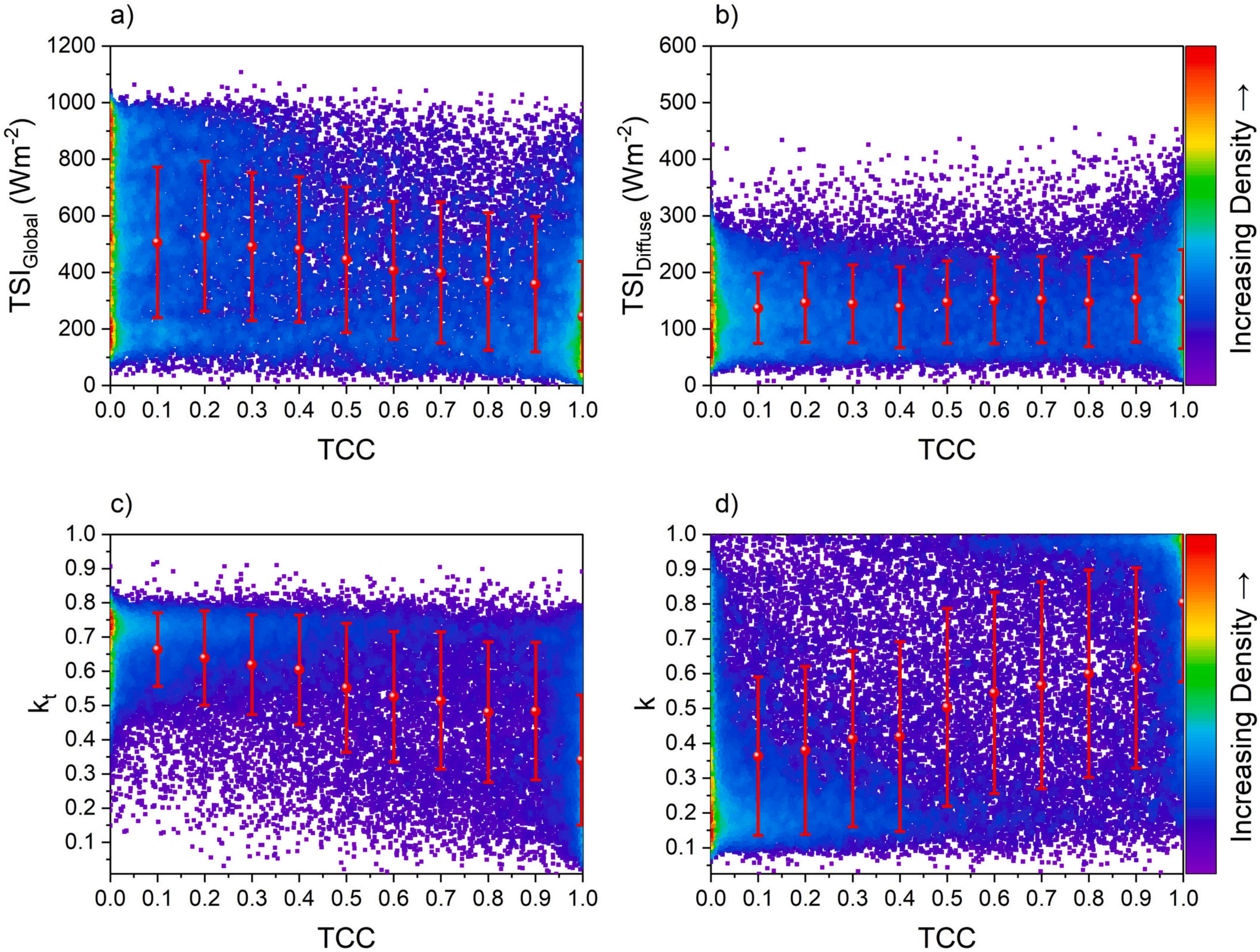

Fig. 6. Relationship between TSI_{Global} (left) or $TSI_{Diffuse}$ (right) versus TCC (upper panels), and between k_t (right) or k (right) versus TCC (lower panels) at Granada during the entire study period (2008–2018). The red dots and red bars represent the average and standard deviation values at the TCC values indicated. (For interpretation of the references to colour in this figure legend, the reader is referred to the web version of this article.)

the surface, but also on the distribution of its components (direct and diffuse), and specially on the transparency of the atmosphere to the direct component of TSI, since the computed slope (not shown in the figure) for its relationship with TCC is -270 ± 30 Wm^{-2} ($r^2 = 0.90$) and 15 ± 4 Wm^{-2} ($r^2 = 0.65$) for TSI_{Global}, and $TSI_{Diffuse}$, respectively.

4.3. Cloud radiative effects

Fig. 7 represents boxplots for CRF_{Global} and $CRF_{Diffuse}$, computed by Eq. (11), positive values mean warming effect on the surface due to an increase in the availability of solar radiation, while negative values

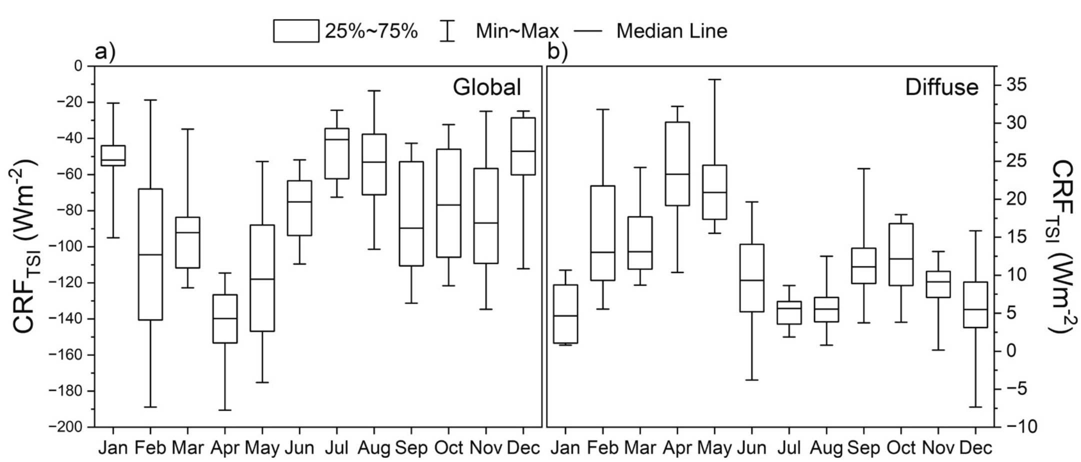

Fig. 7. CRF_{Total} annual statistics for 2008–2018: (a) Global and (b) Diffuse component. Bars correspond to the minimum and maximum values. The box limits are the 75th and 25th percentiles and the midline is the median.

imply the opposite effect. The average values for the full study period is about -80 ± 30 Wm^{-2} for $CRF_{TSI,Global}$ and 11 ± 6 Wm^{-2} for $CRF_{TSI,Diffuse}$. Both boxplots show a clear seasonal pattern: two increasing trends in spring and autumn (January to April and July to September/October), and two decreasing trends during summer and winter (April to July and September/October to December), in absolute values; this pattern was also found by Lozano et al. (2022) and Trisolino et al. (2018) for the PAR range. Therefore, $CRF_{TSI,Global}$ reaches its maximum value (in absolute terms) in April of -137.4 Wm^{-2} and its minimum value in July of -37.6 Wm^{-2}, meanwhile $CRF_{TSI,Diffuse}$ reaches the maximum value of 22.6 Wm^{-2} also found in April, and its minimum value of 4.4 Wm^{-2} in January. The behaviour of the seasonal pattern, found in the $CRF_{TSI,Diffuse}$ analysis, with two maximum values in spring and autumn and two minimum values in summer and winter, is related to the total column cloud ice content in which the same pattern can be found (see Fig. 4e in Lozano et al., 2022), and is also confirmed by the high clouds occurrence in the same period and site (see Fig. 4b in Lozano et al., 2022), since high clouds are mainly composed of ice particles (Liou et al., 2008; Luebke et al., 2016). Secondly, the behaviour found for CRF_{Global} is due to more complex interactions not only associated with the occurrence of highest clouds and the ice content but also with the cloud opacity and overcast occurrence that are more frequent in spring and autumn in this Mediterranean area. On the other hand, the same patterns in CRF_{Global} and $CRF_{Diffuse}$ were found in the same period and site by Lozano et al. (2022) in their analysis in the PAR range, and also in other areas in the Mediterranean basin: Trisolino et al. (2018) for the PAR range, and Pyrina et al. (2015), for the shortwave range, have related the maximum value of CRF in April to the higher cloud optical thickness in the same month. Other authors have computed CRF by using radiative transfer models (RTM), Pyrina et al. (2015) found an average value of -43.7 Wm^{-2} for the Mediterranean basin in the shortwave range, and for a period of 24 years (1984–2007) by employing a spectral RTM for calculations. Alexandri et al. (2021) using the Santa Barbara DISORT Atmospheric Radiative Transfer (SBDART) model found a value of -36 Wm^{-2} for liquid clouds and -19 Wm^{-2} for ice clouds in a period of 15 years (2005–2019) in Greece.

On the other hand, since clouds are considered one of the most important factors controlling climate and exert a net cooling effect on shortwave radiation by reflection of solar radiation it is interesting to analyse the annual CRF evolution. In that sense, Fig. 8 shows the annual evolution of CRF_{TSI} and CRF_{PAR} for both Global and Diffuse components, where a clear decreasing trend (in absolute terms) is found for both wavelength ranges and both solar radiation components, CRF_{TSI} shows a slope of 1.22 Wm^{-2} year^{-1} and $-$ 0.37 Wm^{-2} year^{-1}, and about 0.52 Wm^{-2} year^{-1} and $-$ 0.42 Wm^{-2} year^{-1} for CRF_{PAR}, in the global and diffuse component, respectively. It is interesting to note that all slopes are significant with a *p*-value below 0.001. The main finding is that clouds are exerting less cooling effects in this Mediterranean site over time. In the same site and period Lozano et al. (2021) also found a downward trend on aerosol radiative effects of 2.66 Wm$^{-2}\tau^{-1}$ year^{-1}. Therefore, these findings reveal together a weakening of the main atmospheric cooling mechanisms in this Mediterranean area over time.

5. Conclusions

This study is the last part of a series of three research papers spanning an eleven-year period (2008–2018) at a mid-latitude urban site in the Mediterranean basin located in the southeast of Spain. During the previous works, the radiative effects of aerosols and clouds on the surface were analysed in detail, both in the PAR and in the TSI. For this purpose, a complete characterization of the TSI was carried out in the present work. Secondly, the effects of sky conditions on solar radiation in the solar spectrum were analysed through two parameters: the clearness index (k_t) and the Total Cloud Cover (TCC). Finally, a comparative analysis between global and diffuse CRF, defined as the difference between solar radiation under all and clear sky conditions, in both the TSI and PAR ranges, were evaluated, including a trend analysis over time.

A clear seasonal pattern was observed for both, TSI_{Global} and $TSI_{Diffuse}$, with average values for the entire period of the study of 450 $\pm$ 100 Wm^{-2} and 530 $\pm$ 110 Wm^{-2} for TSI_{Global} under both sky conditions (all and clear), respectively, meaning a 20% less value under all sky conditions in comparison to that for clear skies. Meanwhile $TSI_{Diffuse}$ was quite the opposite as expected, i.e., average values estimated at141 $\pm$ 21 Wm^{-2} and 130 $\pm$ 21 Wm^{-2} for all and clear sky conditions, respectively, implying a 9% higher value for all sky conditions with respect to that for clear skies. On the other hand, we found a relatively low interannual variability, with values of 10% and 7% under all and clear sky conditions, for TSI_{Global}, and up to 11% and 9% for $TSI_{Diffuse}$, implying a maximum interannual variation in the solar spectrum in the entire 11-year period (up to 11%).

The values observed for $CRF_{TSI,Global}$ and $CRF_{TSI,Diffuse}$ also showed a seasonal pattern with a very high variability. In absolute terms, the

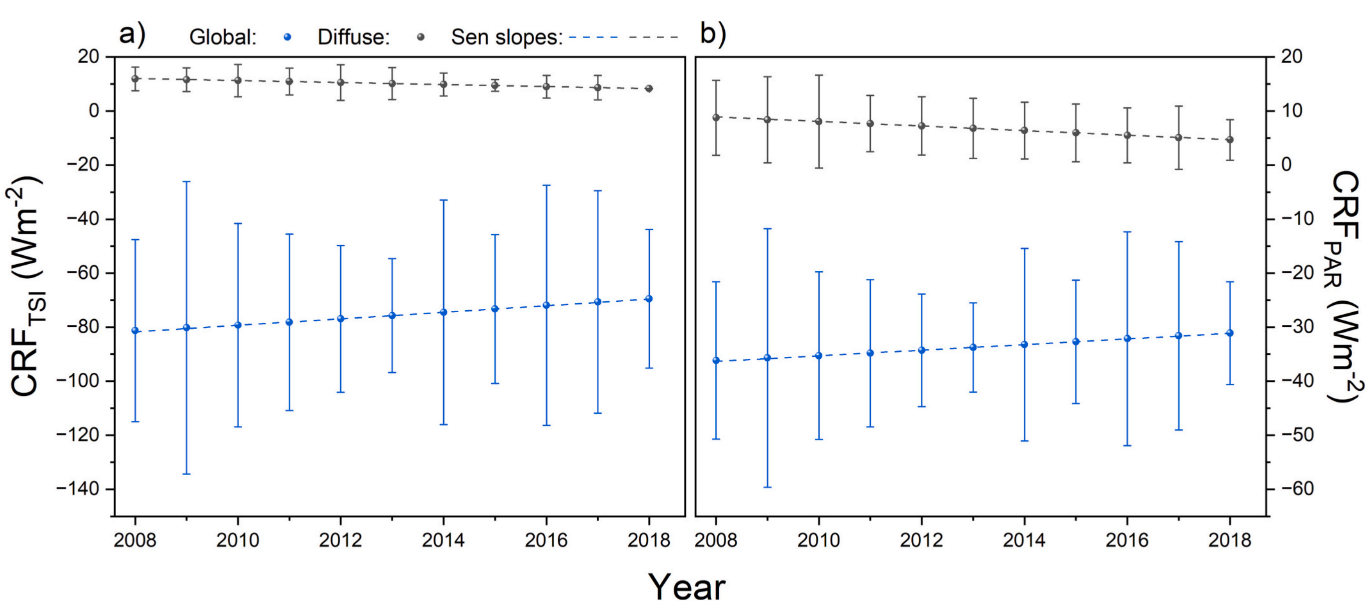

Fig. 8. Yearly cloud radiative forcing (CRF) evolution on the surface for (a) TSI and (b) PAR ranges, for Global and its Diffuse component. Dashed lines point out the linear trends evaluated by the Sen method.

maximum values were found in April reaching values of −137.4 Wm^{-2} for $CRF_{TSI,Global}$ and 22.6 Wm^{-2} $CRF_{TSI,Diffuse}$, meanwhile the minimum values were found in July and January, for $CRF_{TSIGlobal}$ (−37.6 Wm^{-2}) and $CRF_{TSI,Diffuse}$, (4.4 Wm^{-2}), respectively. The seasonal pattern showed two maximum values for both (spring and autumn) in absolute terms. The $CRF_{TSI,Diffuse}$ pattern can be related to the occurrence of high clouds and with the ice water content of clouds, while $CRF_{TSI,Global}$ is related to the opacity of the clouds and the overcast sky occurrence.

Finally, it is interesting to note that in our annual evolution analysis of CRF, the slope observed for both global and diffuse CRF were significant for both wavelength ranges, TSI and PAR, reaching values of 1.22 Wm^{-2} $year^{-1}$ and − 0.37 Wm^{-2} $year^{-1}$ for CRF_{TSI}, and about 0.52 Wm^{-2} $year^{-1}$ and − 0.42 Wm^{-2} $year^{-1}$ for CRF_{PAR}, for the global and the diffuse components, respectively. The positive sign in the slope for CRF_{Global} and the negative sign for $CRF_{Diffuse}$ found in both wavelength ranges (TSI and PAR) has the following interpretation for this Mediterranean site: clouds are exerting less cooling effects over time in accordance with Lozano et al.'s (2021) finding that aerosols are also losing their cooling effects at this site, an evidence of climate change at this site.

Author contributions

Conceptualization, I.F.M and I.L.L.; Formal analysis, I.L.L., I.A.A and I.F.M.; Investigation, I.F.M., I.L.L., and I.A.A.; Methodology, I.F.M, and I.LL.; Resources, I.F.M; Supervision, I.F.M.; Visualization, I.L.L.; Writing original draft, I.L.L, I.F.M., and I.A.A. All authors have read and agreed to the published version of the manuscript.

Declaration of Competing Interest

The authors declare that they have no known competing financial interests or personal relationships that could have appeared to influence the work reported in this paper.

Data availability

Data will be made available on request.

Acknowledgments

This work was supported by the Spanish Ministry of Economy and Competitiveness through projects CGL2017-90884-REDT, PID2020-120015RB-I00, ID2020-117825GB-C21, PID2020-117825GB-C22 and PID2021-128008OB-I00, by the Andalusia Regional Government, University of Granada and FEDER funds through project B-RNM-524-UGR20, P20-00136 and P18-RT-3820. This research was partially supported by the Scientific Units of Excellence Program (grant no. UCE-PP2017-02). The authors thankfully acknowledge the FEDER program for the instrumentation used in this work. Open Access funding provided by University of Helsinki.

Appendix A. Supplementary data

Supplementary data to this article can be found online at https://doi.org/10.1016/j.atmosres.2023.107072.

References

Alados, I., Alados-Arboledas, L., 1999. Direct and diffuse photosynthetically active radiation: Measurements and modelling. Agric. For. Meteorol. 93 (1) https://doi.org/10.1016/S0168-1923(98)00107-5. Article 1.

Alados-Arboledas, L., Müller, D., Guerrero-Rascado, J.L., Navas-Guzmán, F., Pérez-Ramírez, D., Olmo, F.J., 2011. Optical and microphysical properties of fresh biomass burning aerosol retrieved by Raman lidar, and star-and sun-photometry. Geophys. Res. Lett. 38 (1), Article 1. https://doi.org/10.1029/2010GL045999.

Alexandri, G., Georgoulias, A.K., Balis, D., 2021. Effect of Aerosols, Tropospheric NO2 and Clouds on Surface Solar Radiation over the Eastern Mediterranean (Greece). Remote Sens. 13 (13) https://doi.org/10.3390/rs13132587. Article 13.

Badarinath, K.V.S., Kharol, S.K., Kaskaoutis, D.G., Kambezidis, H.D., 2007. Case study of a dust storm over Hyderabad area, India: its impact on solar radiation using satellite data and ground measurements. Sci. Total Environ. 384(1), Article 1 https://doi.org/10.1016/j.scitotenv.2007.05.031.

Barker, H.W., 2008. Representing cloud overlap with an effective decorrelation length: an assessment using CloudSat and CALIPSO data. J. Geophys. Res. Atmos. 113 (D24) https://doi.org/10.1029/2008JD010391. Article D24.

Batlles, F.J., Olmo, F.J., Alados-Arboledas, L., 1995. On shadowband correction methods for diffuse irradiance measurements. Sol. Energy 54 (2), Article 2. https://doi.org/10.1016/0038-092X(94)00115-T.

Buffoni, L., Maugeri, M., Nanni, T., 1999. Precipitation in Italy from 1833 to 1996. Theor. Appl. Climatol. 63 (1) https://doi.org/10.1007/s007040050089. Article 1.

Burkey, J., 2020. *A Non-parametric Monotonic Trend Test Computing Mann-Kendall Tau, Tau-b, and Sen's Slope Written in Mathworks-MATLAB Implemented Using Matrix Rotations* (1.15.0.2). King County, Department of Natural Resources and Parks, Science and Technical Services Section, Seattle, Washington. USA. http://www.mathworks.com/matlabcentral/fileexchange/authors/23983.

Cariñanos, P., Foyo-Moreno, I., Alados, I., Guerrero-Rascado, J.L., Ruiz-Peñuela, S., Titos, G., Cazorla, A., Alados-Arboledas, L., Díaz de la Guardia, C., 2021. Bioaerosols in urban environments: Trends and interactions with pollutants and meteorological variables based on quasi-climatological series. J. Environ. Manag. 282, 111963 https://doi.org/10.1016/j.jenvman.2021.111963.

Cazorla, A., Casquero-Vera, J.A., Román, R., Guerrero-Rascado, J.L., Toledano, C., Cachorro, V.E., Orza, J.A.G., Cancillo, M.L., Serrano, A., Titos, G., Pandolfi, M., Alastuey, A., Hanrieder, N., Alados-Arboledas, L., 2017. Near-real-time processing of a ceilometer network assisted with sun-photometer data: monitoring a dust outbreak over the Iberian Peninsula. Atmos. Chem. Phys. 17 (19) https://doi.org/10.5194/acp-17-11861-2017. Article 19.

Cohan, D.S., Xu, J., Greenwald, R., Bergin, M.H., Chameides, W.L., 2002. Impact of atmospheric aerosol light scattering and absorption on terrestrial net primary productivity. Glob. Biogeochem. Cycles 16 (4), Article 4. https://doi.org/10.1029/2001GB001441.

Copernicus Climate Change Service (C3S), 2017. ERA5: Fifth generation of ECMWF atmospheric reanalysis of the global climate. Copernicus Climate Change Service Climate Data Store (CDS). https://cds.climate.copernicus.eu/cdsapp#!/home.

Delgado-Capel, M.J., Cariñanos, P., Escudero-Viñolo, M., 2023. Capacity of urban green infrastructure spaces to ameliorate heat wave impacts in Mediterranean compact cities: case study of Granada (South-Eastern Spain). Land 12 (5). https://doi.org/10.3390/land12051076. Article 5.

Eastman, R., Warren, S.G., 2013. A 39-Yr survey of cloud changes from land stations worldwide 1971–2009: long-term trends, relation to aerosols, and expansion of the tropical belt. J. Clim. 26 (4), 1286–1303. https://doi.org/10.1175/JCLI-D-12-00280.1.

Fernández, A.J., Sicard, M., Costa, M.J., Guerrero-Rascado, J.L., Gómez-Amo, J.L., Molero, F., Barragán, R., Basart, S., Bortoli, D., Bedoya-Velásquez, A.E., Utrillas, M.P., Salvador, P., Granados-Muñoz, M.J., Potes, M., Ortiz-Amezcua, P., Martínez-Lozano, J.A., Artíñano, B., Muñoz-Porcar, C., Salgado, R., Pujadas, M., 2019. Extreme, wintertime Saharan dust intrusion in the Iberian Peninsula: Lidar monitoring and evaluation of dust forecast models during the February 2017 event. Atmos. Res. 228, 223–241. https://doi.org/10.1016/j.atmosres.2019.06.007.

Foyo-Moreno, I., Alados, I., Alados-Arboledas, L., 2018. A new empirical model to estimate hourly diffuse photosynthetic photon flux density. Atmos. Res. 203, 189–196. https://doi.org/10.1016/j.atmosres.2017.12.012.

Garcia-Herrera, R.F., Lionello, P., Ulbrich, U., 2014. Preface: understanding dynamics and current developments of climate extremes in the Mediterranean region. Nat. Hazards Earth Syst. Sci. 14 (2) https://doi.org/10.5194/nhess-14-309-2014. Article 2.

Gonsamo, A., Croft, H., Chen, J.M., Wu, C., Froelich, N., Staebler, R.M., 2015. Radiation contributed more than temperature to increased decadal autumn and annual carbon uptake of two eastern North America mature forests. Agric. For. Meteorol. 201, 8–16. https://doi.org/10.1016/j.agrformet.2014.11.007.

Gu, L.H., Baldocchi, D., Verma, S.B., Black, T.A., Vesala, T., Falge, E.M., Dowty, P.R., 2002. Advantages of diffuse radiation for terrestrial ecosystem productivity. J. Geophys. Res.-Atmos. 107 (D5-6) https://doi.org/10.1029/2001JD001242. Article D5-6.

Guerrero-Rascado, J.L., Olmo, F.J., Avilés-Rodríguez, I., Navas-Guzmán, F., Pérez-Ramírez, D., Lyamani, H., Alados Arboledas, L., 2009. Extreme Saharan dust event over the southern Iberian Peninsula in september 2007: active and passive remote sensing from surface and satellite. Atmos. Chem. Phys. 9 (21), Article 21. https://doi.org/10.5194/acp-9-8453-2009.

Harrison, E.F., Minnis, P., Barkstrom, B.R., Ramanathan, V., Cess, R.D., Gibson, G.G., 1990. Seasonal variation of cloud radiative forcing derived from the Earth Radiation Budget Experiment. J. Geophys. Res. Atmos. 95 (D11) https://doi.org/10.1029/JD095iD11p18687. Article D11.

Ianetz, A., Lyubansky, V., Setter, I., Kriheli, B., Evseev, E.G., Kudish, A.I., 2007. Inter-comparison of different models for estimating clear sky solar global radiation for the Negev region of Israel. Energy Convers. Manag. 48 (1), 259–268. https://doi.org/10.1016/j.enconman.2006.04.006.

Iqbal, M., 1983. An Introduction to Solar-Radiation. Bull. Am. Meteorol. Soc. 65 (10). Article 10.

Jacovides, C.P., Boland, J., Asimakopoulos, D.N., Kaltsounides, N.A., 2010. Comparing diffuse radiation models with one predictor for partitioning incident PAR radiation into its diffuse component in the eastern Mediterranean basin. Renew. Energy 35 (8). https://doi.org/10.1016/j.renene.2009.11.015. Article 8.

Jakob, C., Klein, S.A., 2000. A parametrization of the effects of cloud and precipitation overlap for use in general-circulation models. Q. J. R. Meteorol. Soc. 126 (568) https://doi.org/10.1002/qj.49712656809. Article 568.

Jonard, F., De Cannière, S., Brüggemann, N., Gentine, P., Short Gianotti, D.J., Lobet, G., Miralles, D.G., Montzka, C., Pagán, B.R., Rascher, U., Vereecken, H., 2020. Value of sun-induced chlorophyll fluorescence for quantifying hydrological states and fluxes: current status and challenges. Agric. For. Meteorol. 291, 108088 https://doi.org/10.1016/j.agrformet.2020.108088.

Kambezidis, H.D., 2021. The solar radiation climate of Greece. Climate 9 (12). https://doi.org/10.3390/cli9120183. Article 12.

Kambezidis, H.D., Kampezidou, S.I., Kampezidou, D., 2021. Mathematical determination of the upper and lower limits of the diffuse fraction at any site. Appl. Sci. 11 (18) https://doi.org/10.3390/app11188654. Article 18.

Kathilankal, J.C., O'Halloran, T.L., Schmidt, A., Hanson, C.V., Law, B.E., 2014. Development of a semi-parametric PAR (photosynthetically active radiation) partitioning model for the United States, version 1.0. Geosci. Model Dev. 7 (5), Article 5. https://doi.org/10.5194/gmd-7-2477-2014.

Keane, B.J., Ineson, P., Vallack, H.W., Blei, E., Bentley, M., Howarth, S., McNamara, N.P., Rowe, R.L., Williams, M., Toet, S., 2017. Greenhouse gas emissions from the energy crop oilseed rape (Brassica napus); the role of photosynthetically active radiation in diurnal N2O flux variation. GCB Bioenergy 10 (5). https://doi.org/10.1111/gcbb.12491. Article 5.

Kodera, K., Hori, M.E., Yukimoto, S., Sigmond, M., 2008. Solar modulation of the Northern Hemisphere winter trends and its implications with increasing CO2. Geophys. Res. Lett. 35 (3) https://doi.org/10.1029/2007GL031958. Article 3.

Kuo, C.-C., Gan, T.Y., Wang, J., 2020. Climate change impact to Mackenzie river Basin projected by a regional climate model. Clim. Dyn. 54 (7), 3561–3581. https://doi.org/10.1007/s00382-020-05177-7.

Lefèvre, M., Oumbe, A., Blanc, P., Espinar, B., Gschwind, B., Qu, Z., Wald, L., Schroedter-Homscheidt, M., Hoyer-Klick, C., Arola, A., Benedetti, A., Kaiser, J.W., Morcrette, J.-J., 2013. McClear: a new model estimating downwelling solar radiation at ground level in clear-sky conditions. Atmos. Meas. Tech. 6 (9), 2403–2418. https://doi.org/10.5194/amt-6-2403-2013.

Lionello, P., Scarascia, L., 2018. The relation between climate change in the Mediterranean region and global warming. Reg. Environ. Chang. 18 (5), 1481–1493. https://doi.org/10.1007/s10113-018-1290-1.

Lionello, P., Abrantes, F., Gacic, M., Planton, S., Trigo, R., Ulbrich, U., 2014. The climate of the Mediterranean region: research progress and climate change impacts. Reg. Environ. Chang. 14 (5), Article 5. https://doi.org/10.1007/s10113-014-0666-0.

Liou, K.N., Gu, Y., Yue, Q., McFarguhar, G., 2008. On the correlation between ice water content and ice crystal size and its application to radiative transfer and general circulation models. Geophys. Res. Lett. 35 (13), Article 13. https://doi.org/10.1029/2008GL033918.

Liu, F., Wang, X., Wang, C., Zhang, Q., 2021. Environmental and biotic controls on the interannual variations in CO2 fluxes of a continental monsoon temperate forest. Agric. For. Meteorol. 296, 108232 https://doi.org/10.1016/j.agrformet.2020.108232.

Long, C.N., Ackerman, T.P., 2000. Identification of clear skies from broadband pyranometer measurements and calculation of downwelling shortwave cloud effects. J. Geophys. Res. Atmos. 105 (D12) https://doi.org/10.1029/2000JD900077. Article D12.

Lozano, I.L., Sánchez-Hernández, G., Guerrero-Rascado, J.L., Alados, I., Foyo-Moreno, I., 2021. Aerosol radiative effects in photosynthetically active radiation and total irradiance at a Mediterranean site from an 11-year database. Atmos. Res. 255, 105538 https://doi.org/10.1016/j.atmosres.2021.105538.

Lozano, I.L., Sánchez-Hernández, G., Guerrero-Rascado, J.L., Alados, I., Foyo-Moreno, I., 2022. Analysis of cloud effects on long-term global and diffuse photosynthetically active radiation at a Mediterranean site. Atmos. Res. 268, 106010 https://doi.org/10.1016/j.atmosres.2021.106010.

Luebke, A.E., Afchine, A., Costa, A., Grooß, J.-U., Meyer, J., Rolf, C., Spelten, N., Avallone, L.M., Baumgardner, D., Krämer, M., 2016. The origin of midlatitude ice clouds and the resulting influence on their microphysical properties. Atmos. Chem. Phys. 16 (9), 5793–5809. https://doi.org/10.5194/acp-16-5793-2016.

Lukáč, J., 1994. Trend of solar radiation attenuation by atmospheric aerosols. Atmos. Environ. 28 (5), 961–962. https://doi.org/10.1016/1352-2310(94)90254-2.

Lyamani, H., Olmo, F.J., Alcántara, A., Alados-Arboledas, L., 2006a. Atmospheric aerosols during the 2003 heat wave in southeastern Spain I: Spectral optical depth. Atmos. Environ. 40 (33) https://doi.org/10.1016/j.atmosenv.2006.04.048. Article 33.

Lyamani, H., Olmo, F.J., Alcántara, A., Alados-Arboledas, L., 2006b. Atmospheric aerosols during the 2003 heat wave in southeastern Spain II: Microphysical columnar properties and radiative forcing. Atmos. Environ. 40 (33) https://doi.org/10.1016/j.atmosenv.2006.04.047. Article 33.

Lyamani, H., Fernandez-Galvez, J., Perez-Ramirez, D., Valenzuela, A., Anton, M., Alados, I., Titos, G., Olmo, F.J., Alados-Arboledas, L., 2012. Aerosol properties over two urban sites in South Spain during an extended stagnation episode in winter season. Atmos. Environ. 62, 424–432. https://doi.org/10.1016/j.atmosenv.2012.08.050.

Ma, C.C.Y., Iqbal, M., 1984. Statistical comparison of solar radiation correlations monthly average global and diffuse radiation on horizontal surfaces. Sol. Energy 33 (2), Article 2. https://doi.org/10.1016/0038-092X(84)90231-7.

Mann, H.B., 1945. Nonparametric tests against trend. Econometrica 13 (3). https://doi.org/10.2307/1907187. Article 3. JSTOR.

McCree, K.J., 1972. Test of current definitions of photosynthetically active radiation against leaf photosynthesis data. Agric. Meteorol. 10, 443–453. https://doi.org/10.1016/0002-1571(72)90045-3.

Mekic, M., Gligorovski, S., 2021. Ionic strength effects on heterogeneous and multiphase chemistry: Clouds versus aerosol particles. Atmos. Environ. 244, 117911 https://doi.org/10.1016/j.atmosenv.2020.117911.

Meloni, D., Junkermann, W., di Sarra, A., Cacciani, M., De Silvestri, L., Di Iorio, T., Estellés, V., Gómez-Amo, J.L., Pace, G., Sferlazzo, D.M., 2015. Altitude-resolved shortwave and longwave radiative effects of desert dust in the Mediterranean during the GAMARF campaign: indications of a net daily cooling in the dust layer. J. Geophys. Res. Atmos. 120 (8), 3386–3407. https://doi.org/10.1002/2014JD022312.

Mercado, L.M., Bellouin, N., Sitch, S., Boucher, O., Huntingford, C., Wild, M., Cox, P.M., 2009. Impact of changes in diffuse radiation on the global land carbon sink. Nature 458 (7241). https://doi.org/10.1038/nature07949. Article 7241.

Middlemas, E.A., Clement, A.C., Medeiros, B., Kirtman, B., 2019. Cloud radiative feedbacks and El Niño–southern oscillation. J. Clim. 32 (15), 4661–4680. https://doi.org/10.1175/JCLI-D-18-0842.1.

Navas-Guzmán, F., Müller, D., Bravo-Aranda, J.A., Guerrero-Rascado, J.L., Granados-Muñoz, M.J., Pérez-Ramírez, D., Olmo, F.J., Alados-Arboledas, L., 2013. Eruption of the Eyjafjallajökull Volcano in spring 2010: Multiwavelength Raman lidar measurements of sulphate particles in the lower troposphere. J. Geophys. Res. Atmos. 118 (4), Article 4. https://doi.org/10.1002/jgrd.50116.

Ortiz-Amezcua, P., Guerrero-Rascado, J.L., Granados-Muñoz, M.J., Benavent-Oltra, J.A., Böckmann, C., Samaras, S., Stachlewska, I.S., Janicka, Ł., Baars, H., Bohlmann, S., Alados-Arboledas, L., 2017. Microphysical characterization of long-range transported biomass burning particles from North America at three EARLINET stations. Atmos. Chem. Phys. 17 (9), Article 9. https://doi.org/10.5194/acp-17-5931-2017.

Pérez-Ramírez, D., Veselovskii, I., Whiteman, D.N., Suvorina, A., Korenskiy, M., Kolgotin, A., Holben, B., Dubovik, O., Siniuk, A., Alados-Arboledas, L., 2015. High temporal resolution estimates of columnar aerosol microphysical parameters from spectrum of aerosol optical depth by linear estimation: Application to long-term AERONET and star-photometry measurements. Atmos. Meas. Tech. 8 (8) https://doi.org/10.5194/amt-8-3117-2015. Article 8.

Potter, C., Boriah, S., Steinbach, M., Kumar, V., Klooster, S., 2008a. Terrestrial vegetation dynamics and global climate controls. Clim. Dyn. 31 (1), 67–78. https://doi.org/10.1007/s00382-007-0339-5.

Potter, C., Boriah, S., Steinbach, M., Kumar, V., Klooster, S., 2008b. Terrestrial vegetation dynamics and global climate controls in North America: 2001–05. Earth Interact. 12 (8), Article 8. https://doi.org/10.1175/2008EI249.1.

Pyrina, M., Hatzianastassiou, N., Matsoukas, C., Fotiadi, A., Papadimas, C.D., Pavlakis, K. G., Vardavas, I., 2015. Cloud effects on the solar and thermal radiation budgets of the Mediterranean basin. Atmos. Res. 152, 14–28. https://doi.org/10.1016/j.atmosres.2013.11.009.

Rädel, G., Mauritsen, T., Stevens, B., Dommenget, D., Matei, D., Bellomo, K., Clement, A., 2016. Amplification of El Niño by cloud longwave coupling to atmospheric circulation. Nat. Geosci. 9 (2), Article 2. https://doi.org/10.1038/ngeo2630.

Ramanathan, V., Cess, R.D., Harrison, E.F., Minnis, P., Barkstrom, B.R., Ahmad, E., Hartmann, D., 1989. Cloud-radiative forcing and climate: results from the earth radiation budget experiment. Science 243 (4887). https://doi.org/10.1126/science.243.4887.57. Article 4887.

Ramírez-Aliaga, P., Foyo-Moreno, I., Cariñanos, P., 2022. Effects of environmental stress on the pollen viability of ornamental tree-species in the City of Granada (South-Eastern Spain). Forests 13 (12). https://doi.org/10.3390/f13122131. Article 12.

Ridley, B., Boland, J., Lauret, P., 2010. Modelling of diffuse solar fraction with multiple predictors. Renew. Energy 35 (2), Article 2. https://doi.org/10.1016/j.renene.2009.07.018.

Roebroek, C.T.J., Melsen, L.A., Hoek van Dijke, A.J., Fan, Y., Teuling, A.J., 2020. Global distribution of hydrologic controls on forest growth. Hydrol. Earth Syst. Sci. 24 (9), Article 9. https://doi.org/10.5194/hess-24-4625-2020.

Salvador, P., Alonso-Pérez, S., Pey, J., Artíñano, B., de Bustos, J.J., Alastuey, A., Querol, X., 2014. African dust outbreaks over the western Mediterranean Basin: 11-year characterization of atmospheric circulation patterns and dust source areas. Atmos. Chem. Phys. 14 (13) https://doi.org/10.5194/acp-14-6759-2014. Article 13.

Sanchez, G., Serrano, A., Cancillo, M.L., 2017. Modeling the erythemal surface diffuse irradiance fraction for Badajoz, Spain. Atmos. Chem. Phys. 17 (20) https://doi.org/10.5194/acp-17-12697-2017. Article 20.

Schneider, T., Teixeira, J., Bretherton, C.S., Brient, F., Pressel, K.G., Schär, C., Siebesma, A.P., 2017. Climate goals and computing the future of clouds. Nat. Clim. Chang. 7 (1) https://doi.org/10.1038/nclimate3190. Article 1.

Sen, P.K., 1968. Estimates of the regression coefficient based on Kendall's Tau. J. Am. Stat. Assoc. 63 (324) https://doi.org/10.1080/01621459.1968.10480934. Article 324.

Spencer, J.W., 1971. Fourier series reprensentation of the position of the sun. Search 2 (5). Article 5.

Stocker, T.F., Qin, D., Plattner, G.K., Tignor, M., Allen, S.K., Boschung, J., Nauels, A., Xia, Y., Bex, V., Midgley, P.M., 2013. IPCC, 2013. *Climate Change 2013 - The Physical Science Basis. Contribution of Working Group I to the Fifth Assessment Report of the Intergovernmental Panel on Climate Change.* Cambridge University Press, 2013.

Tan, C., Wang, D., Zhou, J., Du, Y., Luo, M., Zhang, Y., Guo, W., 2018. Remotely Assessing Fraction of Photosynthetically active Radiation (FPAR) for Wheat Canopies based on Hyperspectral Vegetation indexes. Front. Plant Sci. 9 https://doi.org/10.3389/fpls.2018.00776.

Thevenard, D.J., Brunger, A.P., 2002a. The development of typical weather years for international locations: Part I, algorithms. ASHRAE Trans. 108, 376. https://www.proquest.com/docview/192556999/citation/58A508CB944D42EFPQ/1.

Thevenard, D.J., Brunger, A.P., 2002b. The development of typical weather years for international locations: Part II, production / Discussion. ASHRAE Trans. 108, 480. https://www.proquest.com/docview/192533440/citation/CFE86F57C0E438APQ/1.

Titos, G., Del Águila, A., Cazorla, A., Lyamani, H., Casquero-Vera, J.A., Colombi, C., Cuccia, E., Gianelle, V., Močnik, G., Alastuey, A., Olmo, F.J., Alados-Arboledas, L., 2017. Spatial and temporal variability of carbonaceous aerosols: Assessing the impact of biomass burning in the urban environment. Sci. Total Environ. 578, 613–625. https://doi.org/10.1016/j.scitotenv.2016.11.007.

Trenberth, K.E., Fasullo, J.T., Kiehl, J., 2009. Earth's Global Energy Budget. Bull. Am. Meteorol. Soc. 90 (3) https://doi.org/10.1175/2008BAMS2634.1. Article 3.

Trisolino, P., di Sarra, A., Anello, F., Bommarito, C., Di Iorio, T., Meloni, D., Monteleone, F., Pace, G., Piacentino, S., Sferlazzo, D., 2018. A long-term time series of global and diffuse photosynthetically active radiation in the Mediterranean: Interannual variability and cloud effects. Atmos. Chem. Phys. *18* (11) https://doi.org/10.5194/acp-18-7985-2018. Article 11.

Warren, S.G., Eastman, R.M., Hahn, C.J., 2007. A survey of changes in cloud cover and cloud types over land from surface observations, 1971–96. J. Clim. 20 (4), 717–738. https://doi.org/10.1175/JCLI4031.1.

Wild, M., 2009. Global dimming and brightening: a review. J. Geophys. Res.-Atmos. 114, D00D16. https://doi.org/10.1029/2008JD011470.

Yu, L., Zhang, M., Wang, L., Qin, W., Jiang, D., Li, J., 2022. Variability of surface solar radiation under clear skies over Qinghai-Tibet Plateau: Role of aerosols and water vapor. Atmos. Environ. 287, 119286 https://doi.org/10.1016/j.atmosenv.2022.119286.

Zou, L., Lin, A., Wang, L., Xia, X., Gong, W., Zhu, H., Zhao, Z., 2016. Long-term variations of estimated global solar radiation and the influencing factors in Hunan province, China during 1980–2013. Meteorog. Atmos. Phys. 128 (2) https://doi.org/10.1007/s00703-015-0410-4. Article 2. Scopus.

Glossary

ACTRIS: Aerosol, Clouds and Trace Gases Research Infrastructure
AEMET: Spanish Meteorology Statal Agency
AGORA: Andalusian Global Observatory
AOD: Aerosol optical depth
AST: Apparent solar time
CRE: Cloud radiative effects
CRE_{TSI} *and* CRE_{PAR}*:* Cloud radiative effects on TSI and PAR ranges, respectively
C3S: Copernicus Climate Change Service
E_0*:* Eccentricity correction factor of the earth orbit
ECMWF: European Centre for Medium-range Weather Forecasts
ERA5: Reanalysis Fifth Generation database
I_{All} *and* I_{Clear}*:* Solar radiation in all- and clear- sky conditions
I_{TOA}*:* Irradiance at the top of the atmosphere
$I_{TOA,PAR}$*:* PAR irradiance on the top of the atmosphere
I_0*:* Solar constant (1367 Wm^{-2})
$I_{0,PAR}$*:* Solar constant in the PAR range (634.40 Wm^{-2})
k: Diffuse fraction of TSI
k_{PAR}*:* Diffuse fraction of PAR
k_t*:* Clearness index for TSI
K'_t*:* Daily clearness index for TSI
$k_{t,PAR}$*:* Clearness index for PAR
$K'_{t,PAR}$*:* Daily clearness index for PAR
kur: Kurtosis
m a.s.l: Meter above sea level
Ma: Maximum
MBE: Mean bias error
Md: Median
Mi: Minimum
P5…P95: Percentiles, 5th … 95th
PAR: Photosynthetic active radiation (400–700 nm)
PAR_{Global} *and* $PAR_{Diffuse}$*:* Global solar irradiance, and diffuse component, both for PAR
r^2*:* Determination coefficient
RMSE: Root mean square error
RTM: Radiative Transfer Model
SBDART: Santa Barbara Disort Atmospheric Radiative Transfer model
SD: Standard deviation
Ske: Skewness
TOA: Top of the atmosphere
TCC: Total cloud cover
TSI: Solar irradiance from 280 to 3000 nm
TSI_{Global} *and* $TSI_{Diffuse}$*:* Global solar irradiance, and diffuse component, both for TSI
UV: Ultraviolet irradiance
α*:* Solar elevation in degrees
θ*:* Solar zenith angle
Ψ *and* Ψ_{PAR}*:* Persistence index and persistence index of PAR